Transparent Microcomposite Films Based on a Ce-Doped Li$_6$Gd(BO$_3$)$_3$ Scintillator for Radiation Detection

Xunsheng Zhou, Cai Lin Wang,* and Yinzhen Wang*

ACCESS | Metrics & More | Article Recommendations | SI Supporting Information

ABSTRACT: Scintillators are widely used for high-energy radiation detection. Hybrid inorganic−organic composite scintillators with high light yields, high light decay rates, excellent stability, and low costs are in great demand. Here, we report a novel scintillator composed of Ce-doped Li$_6$Gd(BO$_3$)$_3$ (LGBO) microphosphors (MPs) and polymethyl methacrylate for X-ray and thermal neutron detection. The Ce-doped LGBO MPs, fabricated using a facile high-temperature solid-state reaction method, exhibit intense blue light at 416 nm under X-ray and UV excitation and have a high photoluminescence quantum yield of ∼63%. More importantly, the composite scintillator based on these MPs has excellent transparency and luminescence intensity. The luminescence integral intensity of composite scintillators is superior to that of commercial CsI:Na under X-ray excitation, and the light yield under thermal neutron irradiation is 21,000 photons/thermal neutron. The scintillation decay time is found to be below 600 ns. The neutron−gamma signal discrimination and neutron detection efficiency of the composite scintillators are acceptable for practical application. There is an excellent separation between neutron and background events. It represents significant improvements in scintillator performances, especially for reliable thermal neutron scintillators that are likely to improve the data qualities of scientific instruments, including charge-coupled device-based imagers and Anger logic-based position-sensitive detectors in neutron user facilities.
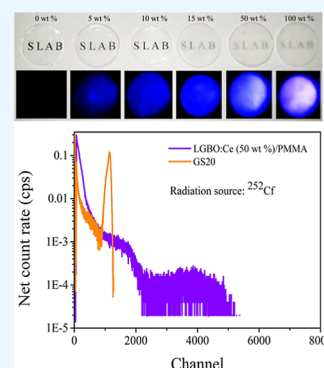
1. INTRODUCTION

Scintillator-based detectors are considerably important in fields including neutron and X-ray scattering science, high-energy physics, medical imaging, and industrial testing and exploration.[1−3] As a core part of the detectors, scintillators convert the energy of high-energy rays or particles into visible photons. A higher light yield, shorter decay time, better stability, and more reasonable production cost have always been pursued in developing these materials.[4] Compared with conventional inorganic scintillation single crystals or transparent ceramics, inorganic particle−polymer composite scintillators not only have easier preparation processes, low cost, and flexibility but also have reasonable performances in detection efficiency, response speed, and so forth.[5,6] Meanwhile, compared to conventional organic scintillators, the addition of inorganic particles increases the effective atomic number (Z_{eff}) of the scintillator, thus improving the ability to stop X-rays and photoelectron production. Inorganic particle−polymer composite scintillators are typically fabricated by combining luminescent quantum dot nanoparticles such as perovskites or CdSe/ZnS composited with organic polymers such as polymethyl methacrylate (PMMA), polystyrene (PS), poly-dimethylsiloxane (PDMS), and so forth.[7−9] For X-ray detection, excellent chemical stability and intense photon emission are required. Quantum dot materials such as perovskites still have problems including poor stability and low loading fraction (<5 wt %) of inorganic nanoparticles in its composite scintillators, which result in a poor attenuation of X-

rays.[5,10] In the field of thermal neutron detection, the light yield, detection efficiency, and decay time of a scintillator are important parameters. In order to capture thermal neutrons, it is necessary to incorporate or contain ^{6}Li, ^{10}B, and ^{157}Gd in the scintillator material. ^{157}Gd has the highest thermal neutron absorption cross-section but suffers from the problem of difficult neutron−gamma discrimination.[11] A common approach is to add ^{6}LiF to the scintillator, as in the typical thermal neutron scintillator ZnS:Ag/^{6}LiF, but this leads to the opaqueness of the materials, further reducing the light yield and neutron detection efficiency.[12]

As a common route for scintillator developments, Ce-doped oxide inorganic microparticles prepared by a high-temperature solid-state reaction may have excellent stability and good scintillation properties. Previously, we have provided a solution to the problem of neutron−gamma discrimination for Ce-doped Gd-containing oxide scintillators in thermal neutron detection.[13,14] However, there are few investigations on the possible applications of Ce-doped Gd-containing oxide inorganic particle−polymer composite scintillators for either
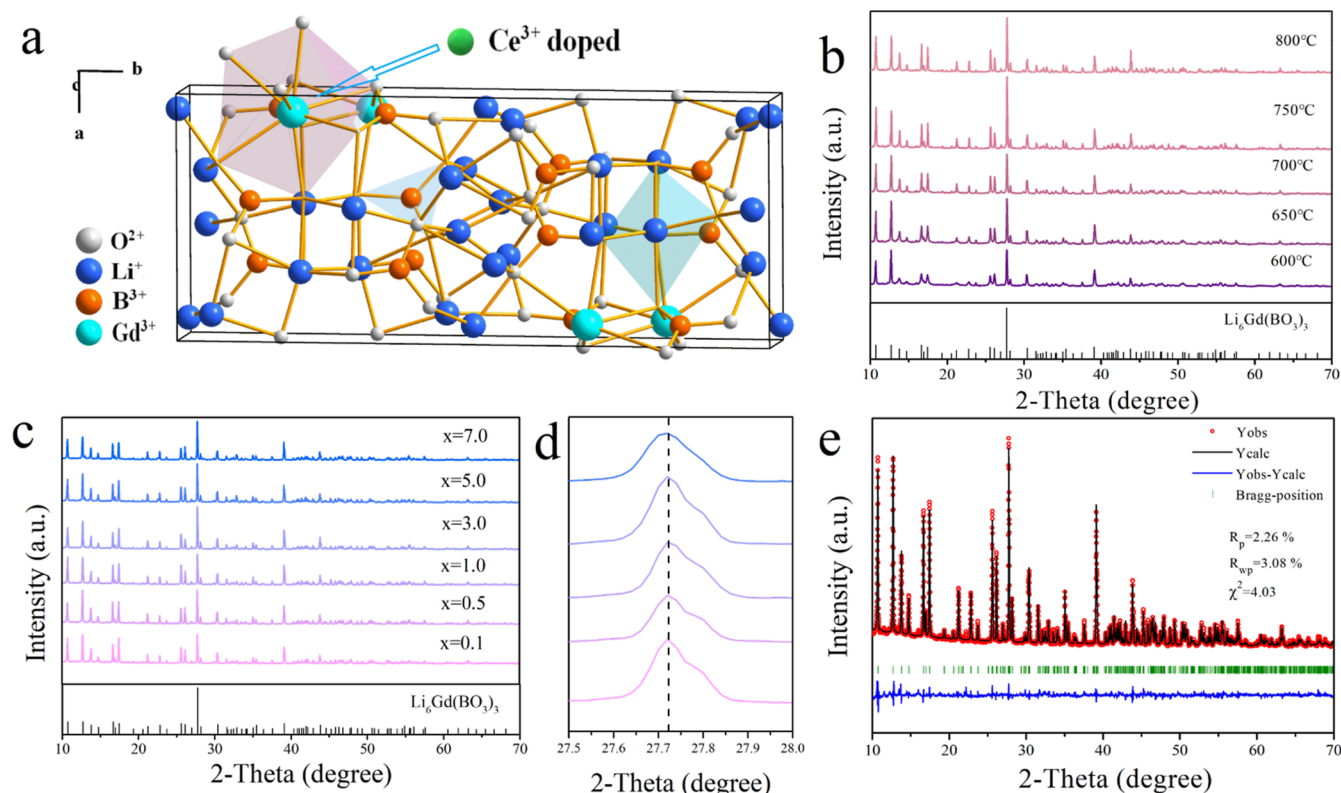
Figure 1. Phases and crystal structures of Ce-doped LGBO. (a) Schematic diagram of the cell structure. (b) XRD patterns of powders with different sintering temperatures (600−800 °C). (c) XRD patterns of powders with different doping concentrations. (d) Enlarged diffraction peaks of (11−2). (e) XRD pattern refinement of 1 mol % CeF$_3$-doped LGBO.

thermal neutron or X-ray detection. Among these oxides, Ce-doped Li$_6$Gd(BO$_3$)$_3$ (LGBO) has a high light yield and short decay time and potentially provides a high detection efficiency and high count rate capability for neutrons or X-rays.[15] The light yields of single crystals under X-ray and thermal neutron irradiation are 14,000 photons/MeV and 40,000 photons/neutron, respectively.[12,16]

In this work, we have investigated a series of samples with different sintering temperatures and doping concentrations in oxides by high-temperature solid-state reactions. Micro-sized phosphors with a high photoluminescence quantum yield (PLQY) and short decay time have been prepared through optimizing sintering conditions and doping concentrations. Luminescence and thermal quenching mechanism of oxide powders are investigated in detail. Furthermore, the obtained powders (n_p = 1.65) were mixed with PMMA (n_m = 1.49) in dichloromethane to obtain films with different phosphor loading fractions. A comprehensive study of the scintillation properties under X-ray, γ-ray, and neutron irradiation was performed. The results indicate that the transparent micro-composite scintillator under X-ray excitation emits intense blue light with wavelengths in the sensitive range of photomultiplier tubes (PMTs); the best of them has a light yield of 21,000 photons/thermal neutron under thermal neutron irradiation. The pulse shape discrimination of neutron/γ is implemented by digital signal processing methods.[13,14] The present work facilitates the development of excellent microcomposite scintillators for the urgent applications in the fields such as neutron/X-ray scattering science, nondestructive industrial tests, medical imaging, and high-energy physics research.

2. EXPERIMENTAL SECTION

2.1. Preparation of Ce-Doped LGBO Microphosphors.
The raw materials were Gd$_2$O$_3$, Li$_2$CO$_3$, H$_3$BO$_3$, and CeF$_3$, all of which have a purity of 99.99%. The raw powdered materials were mixed and ground for 2 h, then were put into an alumina crucible for presintering in a muffle furnace, and were sintered at 400 °C for 8 h. Subsequently, a series of samples were resintered in a muffle furnace at 600−800 °C and sintered again in air for 8 h to optimize the sintering temperature. Another series of samples with different doping concentrations were resintered in a tube furnace at 750 °C and sintered again for 8 h with a reducing gas (8 vol % H$_2$/92 vol % Ar$_2$).

2.2. Preparation of Ce-Doped LGBO/PMMA Composite Scintillators.
The 1 mol % Ce-doped LGBO microphosphor (MP) sintered at 750 °C under a reducing atmosphere was used to prepare composite scintillators. A mixture of 0−0.2 g of the MP and 0.2 g of PMMA was ground for 10 min and transferred to a beaker, and 2 mL of dichloromethane was added. The resulting mixture was stirred in a sonicator for 3−5 min and then poured into circular holes (diameter = 25 mm, depth = 2 mm) of the grinder, and the transparent composite scintillator films with thicknesses of 0.30−0.35 mm were obtained after overnight solidification.

2.3. Characterization.
The crystal structure of the prepared Ce-doped LGBO powders was studied using an X-ray diffractometer (Rigaku, Miniflex 600). The microstructures of the obtained powder and composite scintillators were studied using a scanning electron microscope (Tescan Brno, Vega3). Photoluminescence (PL) and radioluminescence (RL) spectra were measured using a home-built X-ray emission spectra test system shown in Figure S1. Temperature-

dependent emission spectra and PLQY of MPs and composite scintillators were measured using a fluorescence spectrophotometer (Zolix, OmniFluo 900) with an X-ray tube, a heating apparatus, and an integrating sphere. The PLQY was calculated by the following formula

$$\eta = \frac{L_{sam}}{E_{ref} - E_{sam}} \tag{1}$$

where L_{sam}, E_{ref}, and E_{sam} represent the integral intensity of sample emission, reference ($BaSO_4$) scattering, and sample scattering, respectively. The PL decay time was detected using a microscopic ultrafast spectroscopic measurement system (Light Conversion HARPIA). The transmission spectra of the composite scintillators were measured using a UV−vis−NIR absorption spectrometer (Hitachi UH4150).

2.4. Thermal Neutron and Gamma Ray Scintillation Measurements. The pulse-height spectra were measured using a PMT (ET Enterprises, 9124B), a preamplifier (ORTEC, 9305), a shaping amplifier (ORTEC, 572A, 3 μs shaping time), and a multichannel analyzer (MCA, ORTEC, Eesy-MCA-8k). The scintillation decay curves were obtained using an oscilloscope (Agilent, MSO9254A). The measurement details are shown in Figure S2. γ-ray sources were ^{60}Co (average energy = 1.2 MeV) and ^{137}Cs (average energy = 0.662 MeV). A neutron source of ^{252}Cf (9 μg, 1.8×10^8 Bq) was moderated by polyethylene (thickness = 500 mm) to obtain thermal neutrons with an energy-obeying Maxwell distribution (average energy = 25 meV, emission rate ≈ 2000 n/s). The relative light yields under thermal neutron irradiation were calculated using the following equation

$$LY_{LGBO: Ce} = \left(\frac{CN_{LGBO: Ce}}{CN_{GS20}} \right) LY_{GS20}$$

where LY and CN represent the light yield and full energy peak channel number, respectively. Considering that the photons emitted by GS20 and the Ce-doped LGBO/PMMA composite scintillator both originated from the Ce luminescence center and the emission band wavelengths were basically identical (Figure S3), the sensitivity correction factor of PMT was neglected. The neutron−gamma discrimination is performed by our previously proposed pulse-shape algorithms, which has been applied to $Gd_3Al_2Ga_3O_{12}$:Ce (GAGG) scintillators. A detailed explanation can be found in refs 13 and 14.

3. RESULTS AND DISCUSSION

3.1. Crystal Structure and Microscopic Morphology. The cell structure of LGBO is shown in Figure 1a. LGBO is monoclinic with the space group $P2_1/c$. There are three cation positions in the cell, that is, B^{3+}, Li^+, and Gd^{3+}; Ce^{3+} enters the lattice by replacing Gd^{3+} which has a similar radius. The X-ray diffraction (XRD) pattern at different sintering temperatures is shown in Figure 1b. When the sintering temperature is 600 °C, the monoclinic phase of LGBO has been formed. As the sintering temperature increases, the crystallinity and grain size increase, resulting in a gradual increase in the intensity of the diffraction peaks. The intensity of the diffraction peak reaches its maximum at a sintering temperature of 750 °C. As the temperature continues to increase, the intensity of the diffraction peaks decreases, which may be caused by a decrease in crystallinity as the temperature approaches the melting point of LGBO (832 °C, Figure S4). As shown in Figure 1c, all diffraction peaks are consistent with the standard card,

indicating that Ce^{3+} has successfully entered the lattice of the host without forming other crystalline phases. The strongest diffraction peaks are enlarged as shown in Figure 1d; with increasing doping concentration, the diffraction peaks gradually shift toward a smaller angle. According to Bragg's law ($2d \sin \theta = n\lambda$), a larger lattice parameter leads to a smaller angle of the diffraction peak, which indicates that the small-radius Gd^{3+} is replaced by the large-radius Ce^{3+}.[17]

To further investigate the crystalline phase structure of the sample, the XRD pattern of the 1 mol % Ce-doped sample sintered at 750 °C was refined using Fullprof software.[18] As shown in Figure 1e, the diffraction pattern of the sample was well fitted. The refinement yielded cell parameters of a = 7.2237 Å, b = 16.5041 Å, c = 6.6901 Å, and β = 105.362°, which are similar to those in the previous reports.[19]

Figure 2a shows photographs of xCe-doped LGBO/yPMMA (x = 0, 0.01, 0.02, 0.03, 0.10, 0.20 g, y = 0.20 g) composite
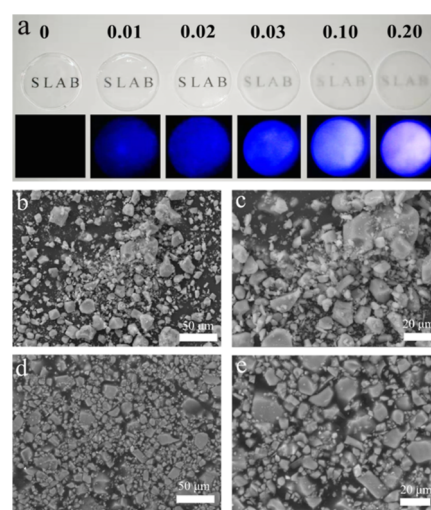

Figure 2. Morphology of the Ce-doped LGBO powder with composite scintillator films. (a) Photographs of scintillator films with different loading fractions (0−0.20 g) under X-ray irradiation. (b,c) SEM photographs of micrometer phosphors. (d,e) SEM photographs of the 10 wt % Ce-doped LGBO/PMMA composite scintillator.

scintillator films under visible light and X-ray irradiation. The luminescence intensity gradually increases with increasing loading, but the transparency decreases. To observe the microscopic morphology of the Ce-doped LGBO MPs and the composite scintillator, scanning electron microscopy (SEM) photographs were taken. As shown in Figure 2b,c, the average size of the micropowder obtained by the high-temperature solid-phase reaction was ∼45 μm (the particle size distribution is shown in Figure S5). An uneven particle size was found, probably due to the uneven distributions of temperature and gas during the sintering process. The microscopic morphology of the Ce-doped LGBO/PMMA composite scintillator is shown in Figure 2d,e. The LGBO luminescent micropowder particles are uniformly distributed in PMMA by mixing with an organic solvent.

3.2. Luminescence Properties. Emission spectra under X-ray excitation and steady-state and transient fluorescence spectra were used to analyze the luminescence properties of Ce-doped LGBO phosphors. The emission spectra of 1 mol % Ce-doped LGBO phosphors with different sintering temper-
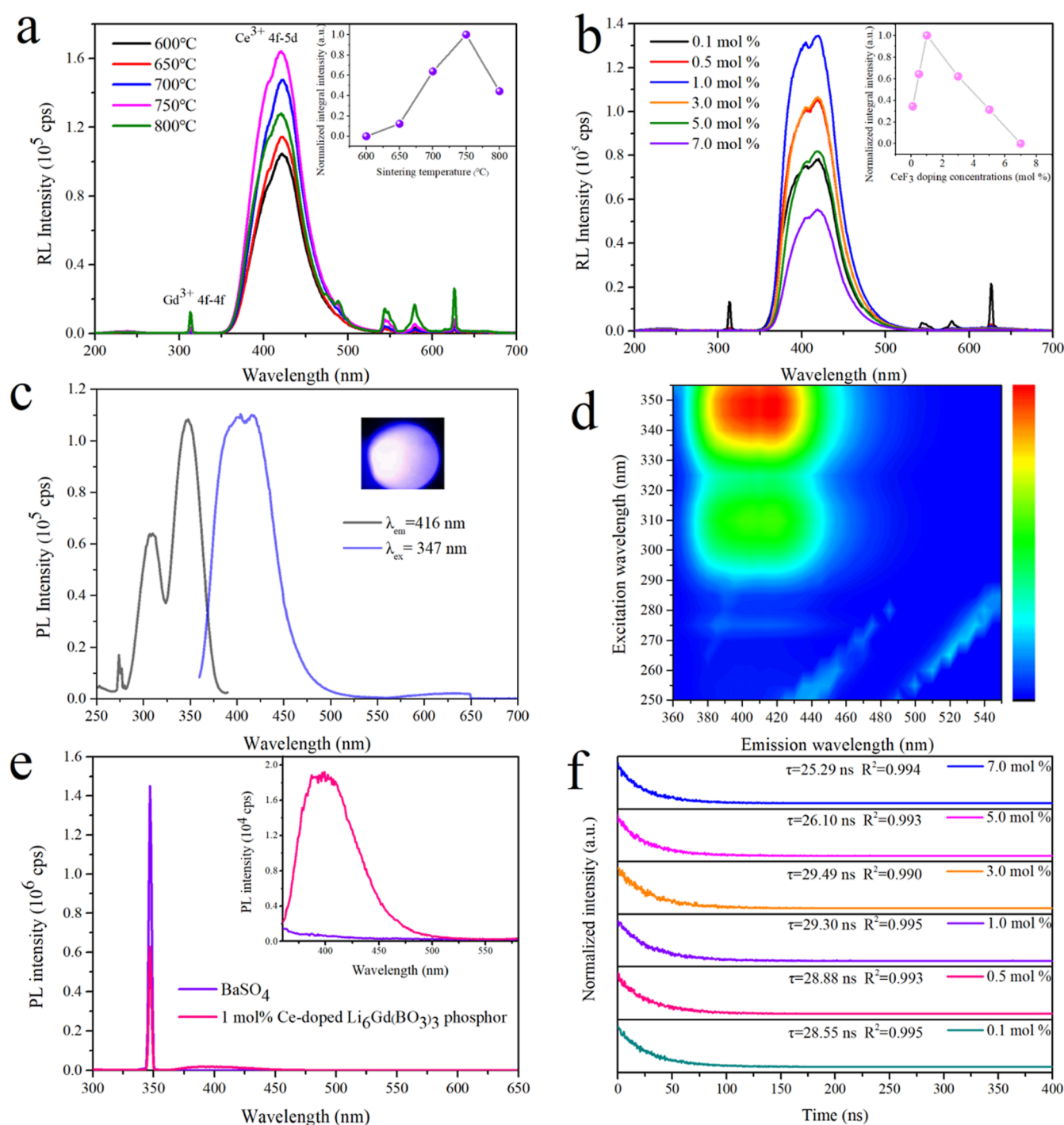
Figure 3. Luminescence properties of Ce-doped LGBO phosphors. (a) Emission spectra of phosphors with different sintering temperatures for X-ray excitation. (b) Emission spectra of phosphors with different CeF_3 doping concentrations for X-ray excitation. (c) Excitation and emission spectra; (d) 3D spectrum; and (e) quantum efficiency measurement spectra of 1 mol % Ce-doped LGBO phosphors. (f) PL decay time for different CeF_3 doping concentrations.

atures under X-ray excitation are shown in Figure 3a. The four emission peaks are located at 313, 421, 544, and 626 nm, respectively. The 313 nm emission peak is attributed to the transition of the Gd^{3+} ion $^6P_J \rightarrow {}^8S_{7/2}$. Similar emission peaks of Gd^{3+} ions are also observed for Gd-containing host materials.[20] The broad emission peak at 350−550 nm originates from the radiative transitions of the excited state of Ce^{3+}, which can be produced by the absorption of holes by

Ce^{3+} or electrons by Ce^{4+}. The corresponding processes are described as follows.[20]

$$Ce^{3+} + h \rightarrow Ce^{4+}$$

$$Ce^{4+} + e^- \rightarrow (Ce^{3+})^*$$

$$(Ce^{3+})^* \rightarrow Ce^{3+} + h\nu$$
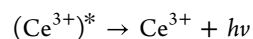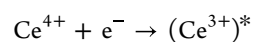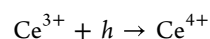
Meanwhile, emission peaks at 544, 579, and 626 nm were also observed, which may be attributed to impurity rare-earth
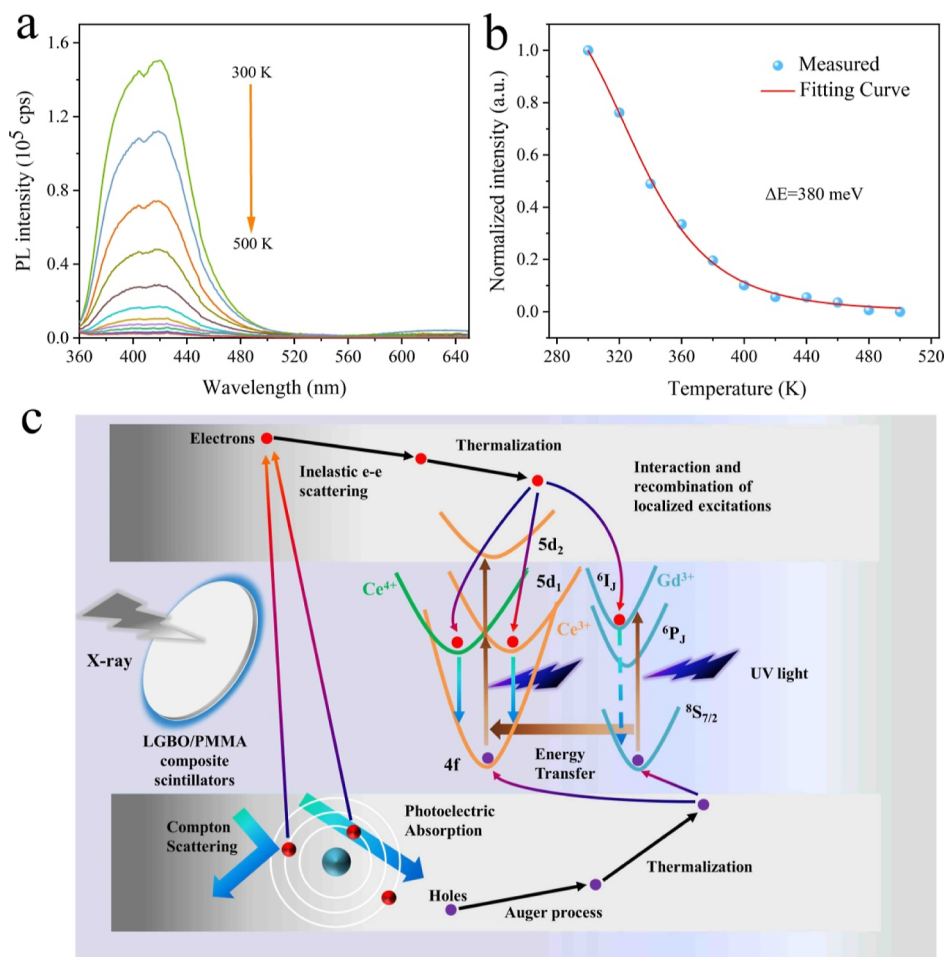
Figure 4. Mechanistic diagram of variable-temperature PL with scintillation and PL processes: (a) emission spectra of 347 nm excitation at different temperatures. (b) Integrated intensity of the emission spectra at different temperatures and its fitting. (c) Schematic diagram of the PL and scintillation processes.

ions, the exact cause of which is still under study. With the increase in sintering temperature, the intensity of the Ce³⁺/Ce⁴⁺ ion emission peak gradually increases and then decreases, and the luminescence intensity reaches a maximum when the sintering temperature is 750 °C. This regularity is consistent with the variation in the XRD peak intensity at different sintering temperatures (Figure 1b), indicating that the luminescence intensity is influenced by the crystallinity and grain size.[21] With the fixed amount of the doping concentration, the more the crystallization, the brighter the emission will be. The emission spectra of Ce-doped LGBO with different doping concentrations are shown in Figure 3b, and the same four emission peaks consistent with Figure 3a are observed. With the increase in doping concentration, the intensity of the emission peak reaches its maximum at a doping concentration of 1 mol %. According to the Forster−Dexter theory, an excessive doping concentration will lead to the intensification of energy transfer between ions, which in turn results in concentration quenching.[22,23]

Figure 3c shows the excitation and emission spectra of 1 mol % Ce-doped LGBO. Three peaks exist in the excitation spectrum, located at 274, 310, and 347 nm, which are consistent with the excitation spectra of Ce-doped LGBO single crystals reported in the literature.[24] The excitation peak at 274 nm corresponds to the $^8S_{7/2} \rightarrow \,^6I_J$ transition of the Gd³⁺ ion and those at 310 and 347 nm correspond to the $4f \rightarrow 5d_2$ and $4f \rightarrow 5d_1$ transitions of the Ce³⁺ ion, respectively. The 350−550 nm broad emission peaks were obtained under UV excitation at 347 nm in general accordance with the X-ray excitation. The three-dimensional (3D) fluorescence spectrum corresponding to excitation and emission is shown in Figure 3d.

To investigate the luminescence performance of Ce-doped LGBO, the PLQY test was performed, as shown in Figure 3e. The calculated PLQY was 62.66%. This indicates that the prepared micrometer-sized Ce-doped LGBO has a high PL quantum efficiency. The light yield is calculated according to the following equation[25]

$$Y = \frac{E}{\beta E_{gap}} SQ$$

where Y is the scintillator light yield, E is the energy absorbed by the scintillator, β is a parameter indicating the average energy required to produce a thermalized electron−hole pair, E_{gap} is the band gap energy value of the host material, S is the energy transfer efficiency of the thermalized electron−hole pair to the excited state of the luminescence center, and Q is the PLQY of the luminescence center. Based on eq 1, a high PLQY may result in a high scintillator light yield. The lifetimes of Ce³⁺ in different host materials are variable due to the
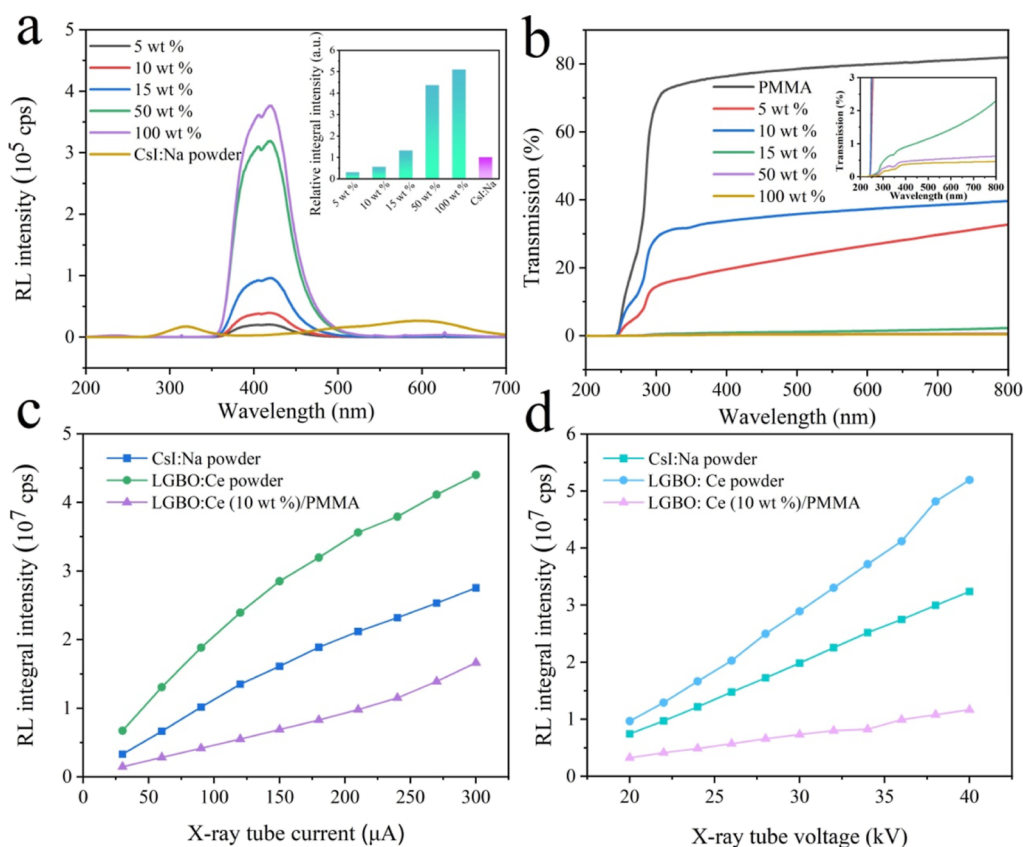
Figure 5. X-ray scintillation properties and transmission spectra of composite scintillators. (a) X-ray emission spectra of scintillators with different loading fractions. (b) Transmission spectra. (c,d) Integrated emission intensity of the Ce-doped LGBO phosphor, composite scintillator, and commercial CsI:Na scintillator at different X-ray tube currents and tube voltage.

influence of the host material crystal field and electron−phonon interactions.

Different applications require different decay times for luminescent materials. For lighting, pc-LEDs are usually required for a long decay time (microsecond to millisecond). While for scintillators, short decay times (1−100 ns) are typically required in order to facilitate the collection of photon signals when the incident flux of high-energy particles is high.[26] Figure 3f shows the doping concentration-dependent PL decay time under UV-pulsed excitation at 347 nm. The decay curves were fitted using the single exponential formula[27]

$$I(t) = A \exp\left(-\frac{t}{\tau}\right)$$

where $I(t)$ is the time-dependent PL intensity, A is the fitting parameter, and τ is the PL decay time. The fitted luminescence lifetimes were obtained in the range of 25.29−29.49 ns (detailed fitting is shown in Figure S6), and the results indicate that the PL of Ce^{3+} in LGBO has a fast decay.

3.3. PL Thermal Quenching, PL, and Scintillation Mechanisms. The thermal stability of the emission centers will determine the scintillation efficiency and light yield under high-temperature conditions.[28] The increase in temperature intensifies electron−phonon coupling and nonradiation transition processes, leading to the thermal quenching of luminescence. In order to investigate the thermal quenching phenomenon of Ce-doped LGBO in detail, the emission spectra at different temperatures were measured. As shown in Figure 4a, the luminescence intensity gradually decreases as the temperature increases from 300 to 500 K. To further analyze

the variation in the luminescence intensity with temperature, the curve of the integrated intensity with temperature was obtained by integrating the emission peaks at different temperatures. According to the current research on the thermal quenching of Ce^{3+} in the literature, the thermal quenching mechanism of Ce^{3+} is mainly in the form of crossover relaxation and thermal ionization,[29,30] both of which can be fitted using the following equation[31]

$$\frac{I(T)}{I_0} = \left[1 + A \exp\left(-\frac{\Delta E}{k_B T}\right) \right]^{-1}$$

where I_0 is the integrated intensity corresponding to 0 K, $I(T)$ is the integrated intensity at temperature T, A is a constant related to the matrix, k_B is the Boltzmann constant, and ΔE is the thermal quenching activation energy (or thermal ionization energy). Here, we use ΔE to measure the thermal stability of the phosphor. The thermal quenching activation energy of 1 mol % Ce-doped LGBO is 380 meV, as obtained by the fitting, which is very similar to the results of Ogorodnikov et al.[32] The large ΔE indicates its excellent stability. The measurement results of thermoluminescence (TL) spectroscopy showed that no significant emission peak was observed (Figure S7), and considering the large Stokes shift (ΔS = 4780 cm^{-1}), it is believed that the thermal quenching phenomenon is more possibly caused by crossover relaxation.[33]

From the previous results and analysis, combined with the reports in the literature,[33] the model of the Ce^{3+} luminescence process in the LGBO host material is established, as shown in Figure 4c. The left and right sides of Figure 4c correspond to
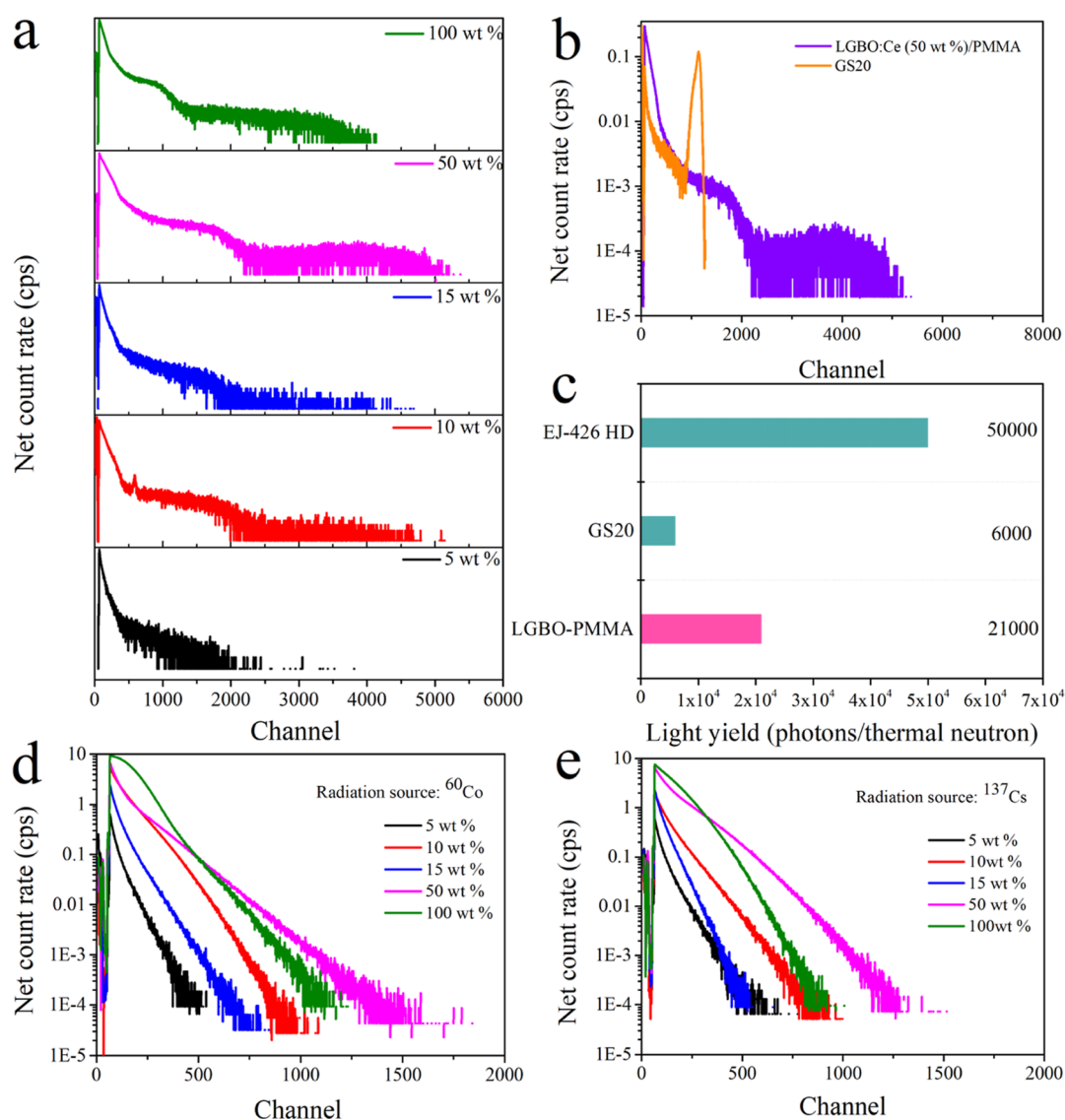
Figure 6. Pulse height spectra of composite scintillators irradiated with different radioactive sources. (a) Pulse height spectra of composite scintillators with different Ce-doped LGBO MP loading fractions under thermal neutron irradiation. (b) Pulse height spectra of the 1 mol % Ce-doped LGBO (50 wt %)/PMMA composite scintillator compared with that of commercial scintillation glass GS20. (c) Light yield of our composite scintillator compared with that of GS20 and a typical commercial scintillation screen EJ-426 HD. (d,e) Pulse height spectra of composite scintillators with different loading fractions under two types of γ-ray irradiation, ^{137}Cs and ^{60}Co, respectively.

the scintillation and fluorescence processes, respectively. For the scintillation process, there are four main steps:[2] absorption of ionizing radiation by the scintillator to generate primary excitation (the photoelectric effect and Compton scattering); production and thermalization of secondary electron−hole pairs (the Auger process and electron inelastic scattering); energy transfer to the luminescence center; and visible light emission. As for the fluorescence process, the host material is usually not involved, and the luminescent centers absorb and emit visible photons directly.

3.4. X-ray Scintillation Performance and the Transmittance of Composite Scintillators. The emission spectra of the Ce-doped LGBO/PMMA composite scintillator with different loading fractions under X-ray excitation are shown in Figure 5a. The luminescence intensity of the composite scintillator increases with the loading fraction. As shown in the inset of Figure 5a, when the phosphor loading fraction exceeds 15 wt %, the RL integrated intensity of the composite

scintillator will be superior to that of the commercial CsI:Na. Figure 5b shows the corresponding transmittance curves. Pure PMMA has a transmittance of about 80% in the 300−800 nm band. The transmittance of the 10 wt % Ce-doped LGBO/ PMMA composite scintillator is close to 40%. Multiple repetitions of samples prepared with different loading fractions showed that the uniformity is poor when the loading amount is 5 wt %, and the transparency is always lower than that of the samples with 10 wt % loading.

To further investigate the X-ray scintillation performance of the Ce-doped LGBO phosphor and composite scintillator, the luminescence intensity versus X-ray tube current and voltage curves were obtained (Figure 5c,d). The 10 wt % Ce-doped LGBO/PMMA composite scintillator was detected to have lower luminescence intensity than the commercial CsI:Na powder due to the comparatively low phosphor loading. A comparison between the phosphors shows that the luminescence intensity of the 1 mol % Ce-doped LGBO phosphor

under X-ray excitation is higher than that of the commercial CsI:Na powder. The integrated luminescence intensity has an essentially linear increase with increasing X-ray tube current and voltage. This indicates that the Ce-doped LGBO/PMMA composite scintillator has potential applications in the radiation detection of X-rays.

3.5. Light Yield. In order to investigate the light yield of composite scintillators in detail, the pulse height spectra of samples with different loading fractions irradiated by different radioactive sources were measured. The pulse distribution of the composite scintillator with different loading fractions under the irradiation of a ^{252}Cf thermal neutron source is shown in Figure 6a. The light yield of the Ce-doped LGBO/PMMA composite scintillator is mainly determined by the transparency and the powder loading fraction. As the content of the Ce-doped LGBO phosphors increases, the cut-off channel number of the pulse height spectra gradually increases, which indicates more pulsed photons of a high amplitude and higher light yield. However, when the loading fraction is 100%, the cut-off channel number of the samples decreases, which is due to a drastic decrease in transparency, and most of the photons are lost by light scattering. The cut-off channel number of the 50 wt % sample can reach 5000, and the channel number of the full energy peak is about 4000.

The other samples failed to observe a significant full energy peak, which may be due to the loss of high-amplitude pulsed photons due to light scattering. To obtain the relative optical yield of the composite scintillator, the pulse height spectrum of the 50 wt % loading fraction sample was compared with that of the commercial scintillator ^{6}Li-glass GS20 (Figure 6b). Based on the GS20 light yield (6000 photons/thermal neutron),[12] a relative light yield of ~21,000 photons/thermal neutron was obtained for the sample with a 50 wt % loading fraction. In addition, the pulse height spectra of samples with different loading fractions were tested under irradiation with ^{60}Co and ^{137}Cs γ-ray sources (Figure 6d,e). The γ-ray light yield varies with the loading fraction in the same pattern as thermal neutrons. Compared to thermal neutrons, the cut-off channel numbers of pulse height spectra of composite scintillators with different loading fractions under γ-ray irradiation are less than 2000.

3.6. Scintillation Decay Time and n−γ Discrimination. In applications involving high count rates of incident particles or time-of-flight measurements, the timing characteristics of the scintillator become essential. Scintillators with a shorter decay time will allow detectors to have a higher count rare capability or higher time resolution. To investigate the scintillation decay time components of the LGBO/PMMA composite scintillator, the decay times under irradiation from different radioactive sources were collected (Figure 7a). All decay variations can be well fitted by the triple exponential function[34]

$$I(t) = A_1\exp\left(-\frac{t}{\tau_1}\right) + A_2\exp\left(-\frac{t}{\tau_2}\right) + A_3\exp\left(-\frac{t}{\tau_3}\right)$$

where $I(t)$ is the time-dependent scintillation light intensity; A_i ($i = 1, 2, 3$) is the fitting parameter; and τ_i ($i = 1, 2, 3$) is the decay time of the fast, intermediate, and slow components, respectively. The decay time components obtained by the fitting are shown in Table 1. The decay time of all three types components can be corresponded to the data reported previously in the literature studies.[34−36] The fast decay
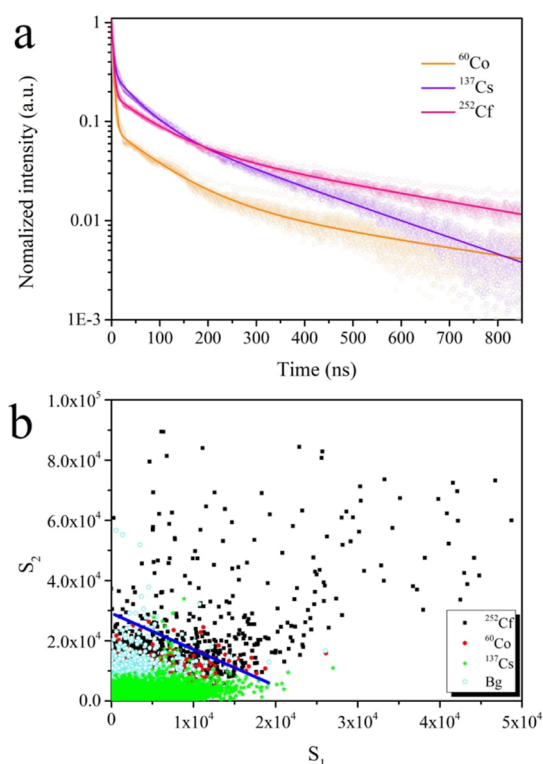
Figure 7. (a) Scintillation decay under irradiation from different radioactive sources and the corresponding fitted curves. (b) Neutron−gamma discrimination for the 50 wt % LGBO phosphor-loaded composite scintillator (S_1−S_2 scatter plot).

Table 1. Scintillation Decay Time Components under the Excitation of Different Radioactive Sources for the 50 wt % LGBO Phosphor-Loaded Composite Scintillator

radiation sources	τ_1 (ns) Ce^{3+}	τ_2 (ns) Ce^{3+}	τ_3 (ns) Gd^{3+} → Ce^{3+}
^{60}Co	3.69 (18%)	95.10 (32%)	594.44 (50%)
^{137}Cs	3.76 (6%)	56.22 (29%)	257.80 (65%)
^{252}Cf	3.60 (7%)	88.19 (25%)	515.93 (68%)

components of 3.60−3.76 ns and the intermediate decay components of 56.22−95.10 ns are attributed to the intrinsic scintillation decay of Ce^{3+} ions, while the slow decay components of 257.80−594.44 ns are attributed to the energy transfer of Gd^{3+} → Ce^{3+}.[36]

For efficient neutron detection, an excellent neutron−gamma discrimination (NGD) ratio (or neutron−gamma efficiency ratio) is required for a practical application such as neutron scattering, security, or nondestructive testing in industry. From the fitting results in Table 1, the decay time components of ^{252}Cf neutrons and ^{60}Co γ-rays are different. The neutron−gamma discrimination using pulse shape difference is performed via a conventional two-feature S_1−S_2 plot,[13] as shown in Figure 7b. Here, S_1 and S_2 are the integration values of individual pulses in the time windows of $[-50, 0]$ ns and $[0, 50]$ ns, respectively. A two-dimensional scatter plot of S_1−S_2 can separate most of the neutron from the γ signal using the blue solid line as the class boundary. The boundary is set to obtain both a neutron efficiency and an NGD ratio as high as possible. Events above and below this line are assigned to neutrons and γ-rays, respectively. However, the conventional S_2−S_1 method can only provide a neutron detection efficiency

of about 1.4% and an NGD ratio of about 10^2, which are too low to have any practical applications.

To improve both the neutron detection efficiency and NGD ratio, we applied a graph-embedded non-negative matrix factorization (GNMF) method for particle discrimination.[14] In this method, an event graph (or network) is established to describe the event similarity using reference events selected from the data measured under ^{252}Cf and ^{60}Co sources and background. A batch of unlabeled events is regarded as graph signals, whose low-dimensional representation is searched under the assumption of smoothness in the high-dimensional-event graph. More description can be found in ref 14. Using the GNMF data model, we found that P_2 versus V_2 can be used to separate neutron events from γ and background events, where V_2 and P_2 are the second components of the signal matrix V and projected matrix $P = LV$ and L is the Laplacian operator of the graph. As shown in Figure 8, a boundary
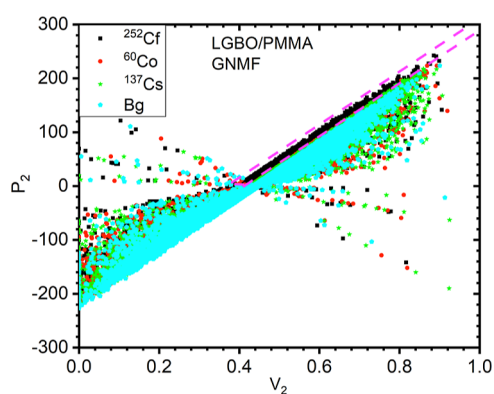
Figure 8. Neutron−gamma discrimination using the GNMF method for the 50 wt % LGBO phosphor-loaded composite scintillator.

composed of three lines can separate neutron and γ. There is an almost clean separation between neutron and background events. A thermal neutron detection efficiency of 55% (relative to a GS20 detector) and an NGD ratio of about 1.3×10^5 are obtained, which are much better than those obtained by the traditional $S_2 - S_1$ method and are good enough for practical applications. Further improvement in the NGD and neutron detection efficiency may reside in the following: (i) the improvement of the average fitting residual value (4.4×10^{-2}) of R^2, which is slightly larger than that for a bright GAGG scintillator.[14] (ii) The optimization of the film thickness, component fractions, and LGBO particle size.

4. CONCLUSIONS

In conclusion, we prepared Ce-doped LGBO MPs with a high stability and high PL quantum efficiency by a facile high-temperature solid-state reaction. These MPs exhibit high luminescence intensity under X-ray and UV excitation and a decay time below 600 ns. We have discussed the PL and scintillation processes in detail and have investigated the mechanism of the luminescence thermal quench phenomenon of Ce^{3+} in the LGBO system. Furthermore, the transparent scintillator films have been fabricated by mixing LGBO MPs with PMMA. A comparison with commercial scintillators CsI:Na and GS20 shows that our scintillator films exhibit high light yields under irradiation with X-rays and thermal neutrons. Due to the large thermal neutron absorption cross-section of ^{157}Gd and the easy solid-state sintering route to obtain MPs,

fabricated Ce-doped LGBO/PMMA scintillators would effectively reduce the production cost and time. Our results suggest that Ce-doped LGBO/PMMA is a low-cost, high-performance scintillator for X-ray and thermal neutron detection.

■ ASSOCIATED CONTENT

ⓢ Supporting Information

The Supporting Information is available free of charge at https://pubs.acs.org/doi/10.1021/acsomega.2c04413.

Schematic diagram of the emission spectra measurements for X-ray excitation, schematic diagram of the pulse height spectra measurements under thermal neutron/γ-ray irradiation, emission spectra of GS20 and the LGBO/PMMA composite scintillator under X-ray excitation, differential thermal analysis curve of pure LGBO powders, particle size distribution of the 1 mol % Ce-doped LGBO phosphor, fluorescence decay curves and fitted curves of samples with different doping concentrations, and TL spectrum of the 1 mol % Ce-doped LGBO phosphor (PDF)

■ AUTHOR INFORMATION

Corresponding Authors

Cai Lin Wang − *Neutron Science Platform, Songshan Lake Materials Laboratory, Dongguan 523808, China;*
Email: clwang@sslab.org.cn

Yinzhen Wang − *Guangdong Provincial Key Laboratory of Quantum Engineering and Quantum Materials, Guangdong Engineering Technology Research Center of Efficient Green Energy and Environmental Protection Materials, School of Physics and Telecommunication Engineering, South China Normal University, Guangzhou 510006, China;*
Email: agwyz@aliyun.com

Author

Xunsheng Zhou − *Neutron Science Platform, Songshan Lake Materials Laboratory, Dongguan 523808, China; Guangdong Provincial Key Laboratory of Quantum Engineering and Quantum Materials, Guangdong Engineering Technology Research Center of Efficient Green Energy and Environmental Protection Materials, School of Physics and Telecommunication Engineering, South China Normal University, Guangzhou 510006, China;* ⓞ orcid.org/0000-0001-8276-612X

Complete contact information is available at:
https://pubs.acs.org/10.1021/acsomega.2c04413

Notes

The authors declare no competing financial interest.

■ REFERENCES

(1) Blasse, G. Scintillator materials. *Chem. Mater.* **1994**, *6*, 1465−1475.

(2) Gektin, A.; Korzhik, M. *Inorganic scintillators for detector systems*; Springer, 2017.

(3) Lin, Z.; Lv, S.; Yang, Z.; Qiu, J.; Zhou, S. Structured Scintillators for Efficient Radiation Detection. *Adv. Sci.* **2022**, *9*, 2102439.

(4) Carini, G.; Denes, P.; Gruener, S.; Lessner, E. *Neutron and X-ray detectors*; USDOE Office of Science (SC): United States, 2012.

(5) Hajagos, T. J.; Liu, C.; Cherepy, N. J.; Pei, Q. High-Z Sensitized Plastic Scintillators: A Review. *Adv. Mater.* **2018**, *30*, No. e1706956.

(6) Hamel, M. *Plastic Scintillators*; Springer, 2021.

(7) Liu, C.; Li, Z.; Hajagos, T. J.; Kishpaugh, D.; Chen, D. Y.; Pei, Q. Transparent Ultra-High-Loading Quantum Dot/Polymer Nanocomposite Monolith for Gamma Scintillation. *ACS Nano* **2017**, *11*, 6422−6430.

(8) Nie, J.; Li, C.; Zhou, S.; Huang, J.; Ouyang, X.; Xu, Q. High Photoluminescence Quantum Yield Perovskite/Polymer Nanocomposites for High Contrast X-ray Imaging. *ACS Appl. Mater. Interfaces* **2021**, *13*, 54348−54353.

(9) Williams, R. T.; Wolszczak, W. W.; Yan, X.; Carroll, D. L. Perovskite quantum-dot-in-host for detection of ionizing radiation. *ACS Nano* **2020**, *14*, 5161−5169.

(10) Gandini, M.; Villa, I.; Beretta, M.; Gotti, C.; Imran, M.; Carulli, F.; Fantuzzi, E.; Sassi, M.; Zaffalon, M.; Brofferio, C.; Manna, L.; Beverina, L.; Vedda, A.; Fasoli, M.; Gironi, L.; Brovelli, S. Efficient, fast and reabsorption-free perovskite nanocrystal-based sensitized plastic scintillators. *Nat. Nanotechnol.* **2020**, *15*, 462−468.

(11) Dumazert, J.; Coulon, R.; Lecomte, Q.; Bertrand, G.; Hamel, M. Gadolinium for neutron detection in current nuclear instrumentation research: A review. *Nucl. Instrum. Methods Phys. Res., Sect. A* **2018**, *882*, 53−68.

(12) van Eijk, C. W. E. Inorganic scintillators for thermal neutron detection. *Radiat. Meas.* **2004**, *38*, 337−342.

(13) Wang, C. Can Ce: Gd₃Al₂Ga₃O₁₂ scintillators detect thermal neutrons? *2019 IEEE Nuclear Science Symposium and Medical Imaging Conference (NSS/MIC)*; IEEE, 2019; pp 1−4.

(14) Wang, C. Gd-containing scintillators for thermal neutron detection via graph-based particle discrimination. *Rev. Sci. Instrum.* **2021**, *92*, 103304.

(15) Fawad, U.; Rooh, G.; Kim, H.; Park, H.; Kim, S.; Khan, S. Scintillation properties of $Li_6Y_{0.5}Gd_{0.5}(BO_3)_3$:$Ce^{3+}$ single crystal. *J. Cryst. Growth* **2015**, *410*, 18−22.

(16) Knitel, M. J.; Dorenbos, P.; van Eijk, C. W. E.; Plasteig, B.; Viana, B.; Kahn-Harari, A.; Vivien, D. Photoluminescence, and scintillation/thermoluminescence yields of several Ce^{3+} and Eu^{2+} activated borates. *Nucl. Instrum. Methods Phys. Res., Sect. A* **2000**, *443*, 364−374.

(17) Bragg, W. H.; Bragg, W. L. The reflection of X-rays by crystals. *Proc. R. Soc. Lond.—Ser. A Contain. Pap. a Math. Phys. Character* **1913**, *88*, 428−438.

(18) Rodríguez-Carvajal, J. FullProf. *CEA/Saclay*: France, 2001.

(19) Zhang, Y.; Chen, X.; Liang, J.; Xu, T. Phase relations of the system Li₂O−Gd₂O₃−B₂O₃ and the structure of a new ternary compound. *J. Alloys Compd.* **2003**, *348*, 314−318.

(20) Khanin, V.; Venevtsev, I.; Chernenko, K.; Pankratov, V.; Klementiev, K.; van Swieten, T.; van Bunningen, A. J.; Vrubel, I.; Shendrik, R.; Ronda, C.; et al. Exciton interaction with Ce^{3+} and Ce^{4+} ions in $(LuGd)_3(Ga,Al)_5O_{12}$ ceramics. *J. Lumin.* **2021**, *237*, 118150.

(21) Wang, W.-N.; Widiyastuti, W.; Ogi, T.; Lenggoro, I. W.; Okuyama, K. Correlations between crystallite/particle size and photoluminescence properties of submicrometer phosphors. *Chem. Mater.* **2007**, *19*, 1723−1730.

(22) Dexter, D. L.; Schulman, J. H. Theory of Concentration Quenching in Inorganic Phosphors. *J. Chem. Phys.* **1954**, *22*, 1063−1070.

(23) Förster, T. Zwischenmolekulare energiewanderung und fluoreszenz. *Ann. Phys.* **1948**, *437*, 55−75.

(24) Singh, A. K.; Singh, S. G.; Tyagi, M.; Desai, D. G.; Sen, S.; Gadkari, S. C. Growth and luminescence properties of Ce doped Li₆Gd(BO₃)₃ single crystals. *AIP Conf. Proc.* **2012**, *1447*, 1337.

(25) Rodnyi, P.; Dorenbos, P.; van Eijk, C. Energy loss in inorganic scintillators. *Phys. Status Solidi B* **1995**, *187*, 15−29.

(26) Knoll, G. F. *Radiation detection and measurement*; John Wiley & Sons, 2010.

(27) Huang, M.; Li, Q. L.; Yuan, R.; Yang, X. C.; Yin, G. Z.; Yang, X. X.; Hu, J. F.; Gao, X. Y.; Deng, Z.; Wang, L.; et al. Improved Phase Stability and Enhanced Luminescence of Calcite Phase $LuBO_3$:Ce^{3+} through Ga^{3+} Incorporation. *Inorg. Chem.* **2020**, *59*, 14513−14525.

(28) Nikl, M.; Yoshikawa, A. Recent R&D trends in inorganic single-crystal scintillator materials for radiation detection. *Adv. Opt. Mater.* **2015**, *3*, 463−481.

(29) Lin, Y.-C.; Bettinelli, M.; Karlsson, M. Unraveling the Mechanisms of Thermal Quenching of Luminescence in Ce^{3+}-Doped Garnet Phosphors. *Chem. Mater.* **2019**, *31*, 3851−3862.

(30) Ueda, J.; Dorenbos, P.; Bos, A. J. J.; Meijerink, A.; Tanabe, S. Insight into the Thermal Quenching Mechanism for $Y_3Al_5O_{12}$:Ce^{3+} through Thermoluminescence Excitation Spectroscopy. *J. Phys. Chem. C* **2015**, *119*, 25003−25008.

(31) Zhou, X.; Wang, B.; Yao, A.; Lu, S.; Hong, Y.; Hu, S.; Cheng, J.; Wang, Y.; Wang, C. Ultraviolet luminescence properties of Te^{4+}-doped $YCa_4O(BO_3)_3$ phosphors. *J. Lumin.* **2021**, *240*, 118458.

(32) Ogorodnikov, I. N.; Poryvai, N. E.; Sedunova, I. N.; Tolmachev, A. V.; Yavetskiy, R. P. Luminescence and thermally stimulated recombination processes in $Li_6Gd(BO_3)_3$:Ce^{3+} crystals. *Opt. Spectrosc.* **2011**, *110*, 266−276.

(33) Ogorodnikov, I. N.; Pustovarov, V. A. Luminescence of impurity-bound excitons in $Li_6GdB_3O_9$:Ce^{3+} single crystals. *J. Phys.: Condens. Matter* **2012**, *24*, 405902.

(34) Fawad, U.; Kim, H.; Park, H.; Kim, S.; Khan, S. Czochralski growth and scintillation properties of $Li_6Lu_xY_{1−x}(BO_3)_3$:Ce^{3+} single crystals. *Nucl. Instrum. Methods Phys. Res., Sect. A* **2016**, *806*, 117−122.

(35) Koroleva, T.; Kidibaev, M.; Nehari, A.; Pedrini, C.; Lebbou, K.; Belsky, A.; Tcherepanov, A.; Ishchenko, A.; Ivanov, V. Y.; Sedunova, I.; Teslenko, O. S.; Viktorov, L. V.; Shulgin, B. V.; Zheng, L. H.; Xu, J.; Kononets, V.; Sidletskiy, O. Ce-doped $Li_6Ln(BO_3)_3$ (Ln=Y, Gd) Single crystals fibers grown by micro-pulling down method and luminescence properties. *Opt. Mater.* **2013**, *35*, 868−874.

(36) Pan, S.; Zhang, J.; Pan, J.; Ren, G.; Li, N.; Wu, Z.; Heng, Y. Optimized crystal growth and luminescence properties of Ce^{3+} ions doped $Li_6Gd(BO_3)_3$, $Li_6Y(BO_3)_3$ and their mixed crystals. *J. Alloys Compd.* **2018**, *751*, 129−137.